Three-dimensional modelling of blur property for conventional optical microscopes

Weihan Hou, Yangjie Wei [*]

Key Laboratory of Intelligent Computing in Medical Image, Ministry of Education, College of Computer Science and Engineering, Northeastern University, Wenhua Street 3, Shenyang 110819, China

ARTICLE INFO

ABSTRACT

Intensity diffusion caused by optical diffraction limits the imaging resolution of conventional optical microscopes, therefore modelling and measuring the intensity transmission and distribution property of the light sources is a significant research topic in system development and pattern recognition. However, the complicated wave propagation process in optical imaging makes it difficult to provide a direct, analytical and simple mathematical model to measure the relationship between the blur degree and various camera parameters. In this study, an improved intensity transmission and distribution calculation method for conventional optical microscopes was proposed; furthermore, a simple mathematical relation between the blur degree and camera parameters was achieved based on the proposed method. First, the light intensity distribution and propagation characteristics of a conventional optical microscope were modeled based on the property of the Fresnel circular hole diffraction combined with the practical optical parameters. Second, by analyzing the property of intensity distribution and blurring imaging, a quantitative simplified mathematical relationship between the blur degree and camera parameters in optical microscope imaging was obtained, and the three-dimensional (3D) blur property in the optical imaging process was analyzed under different conditions. Third, the connection between diffractive optics and geometric optics was obtained by summarizing and generalizing the 3D blur property curve of each monochromatic light source. Finally, the proposed method was verified through a series of simulations and experiments.

1. Introduction

For micro/nano-scale observations, various types of microscopes, including fluorescence [1–3], electron [4,5], and scanning microscopes [6,7], are currently available. Comparatively, conventional optical microscopes have the advantages of being non-destructive, fast and dynamic; therefore, they are an important observation tool in biomedicine, microelectronics, chemistry, and precision instrument manufacturing [8,9].

However, the imaging resolution of optical microscopes is comparatively low due to optical diffraction of the source waves used for illumination [10]. In the geometry optics, the source wave in an optical imaging system is assumed to travel in a straight line; therefore, optical diffraction is negligible, and blur imaging is mainly considered to be the result of defocus due to the limit of the depth-of-field (DOF) of the microscope [11–13]. However, owing to the wave property, the direction of light deviates from a straight

line when it travels around small obstacles or passes through small openings, which is a standard property of all types of waves [14,15]. As the magnification scale of the optical microscope increases, the size of the observed objects and the wavelength of the source wave gradually approach each other, and optical diffraction becomes more obvious than that in the macro-scale cameras. In other words, the source wave passing through the lens scatters in a round spot on the image plane, rather than a focused point, which results in blur imaging similar to defocus. To improve the imaging resolution of optical microscopes at the micro/nano scale, it is necessary to measure the blur imaging properties based on the analysis on the mechanism of light intensity diffusion in an optical imaging system [16].

In the physical optics, the scholars have studied the propagation property of light waves and the modelling of intensity distribution in optical diffraction for many years since Keller first established the geometric theory of optical diffraction in 1962 [16]. Durnin proposed a model for the light intensity distribution of diffraction-free Gaussian beams of different orders under different conditions [17,18]; Sprangle compared the variation of the light intensity distribution of Gaussian and Bessel beams for different parameters [19]; Ruschin proposed a modified Bessel beam model with reduced diffraction phenomena and long distance propagation [20]; Overfelt compared the propagation capabilities and light intensity model variations of Bessel, Gaussian and Bessel-Gaussian beams under the single-hole Fresnel diffraction and Fraunhofer diffraction conditions [21]. These results analyzed the diffraction properties through experiments or simulations, however, their models to calculate the intensity distribution are mostly composed of complicated non-analytical functions, even approximate integral solutions [22–24]. Therefore, it is difficult to simply and quickly analyze the diffraction properties of a practical system. To solve this problem, Wang established a simplified light intensity distribution model for Fresnel diffraction [25]. In contrast to the previous research that focused on divergent waves; in addition, he proposed a mathematical relationship between the divergence and convergent waves and extended his method to calculate the intensity distribution of the convergent waves, which is an important theoretical basis for the intensity analysis during imaging. However, because this research mainly focused on modelling the intensity distribution in an optical diffraction system in free space rather than in an optical imaging system, various camera parameters, such as the length of focus, were not considered. Therefore, it is insufficient to analyze the blur imaging property of an optical imaging system.

On the other hand, because the point spread function (PSF) is an effective factor to evaluate the blur imaging property resulted from intensity distribution, some researchers have proposed many methods to measure the PSF, rather than constructing the complicated intensity distribution model. Generally, the PSF of an optical microscope can be measured by the knife-edge method [26]. To measure the PSF precisely, the knife-edge is perpendicular or parallel to the sampling direction. Although some knife-edge methods have some robustness to the angle of the knife-edge [27], there are still some constraints on the selection of the large-angle knife-edges for optical images. For example, the edge selection at different positions may lead to great difference in PSF measurement [28].

Embedding a sub-resolution microbead sample in optical cement or fixing it on an inclined surface is also an effective method to measure the PSF of a real optical system [29–31], especially for some self-made fluorescence imaging systems that are mostly calibrated with morphological image measurements of fixed-size microbeads [32–34]. However, there are two major challenges to this. First, it is difficult to precisely control the position of a microbead in optical cement, which leads to inaccurate measurement results. Second, human intervention in the optical cement can disrupt the local refractive index in the cement, resulting in an inconsistent refractive index in the optical medium, thus leading to measurement errors. With the exception of experimental methods, some scholars have established a mathematical model to theoretically calculate the PSFs by describing the response of the imaging system through the pupil function of the objective lens in Fourier optics [35–37]. However, these modelling methods are highly complicated and difficult to use for practical optical systems. In addition, the computational accuracy of PSFs is closely related to the modelling of wave energy transmission and diffusion in imaging systems. Although many researchers have proposed powerful methods for relieving the effects of out-of-focus light and diffusion light for many microscope systems [38–41], precise measurement of the blur kernels of a practical high-magnification microscope remains a challenge, because of the complicated imaging process and various dynamic image features at the micro/nano scale. Therefore, it is necessary to construct a continuous mathematical intensity distribution model of a light source and develop a simple and analytical function to measure the blur degree under different camera parameters.

(a) (b)
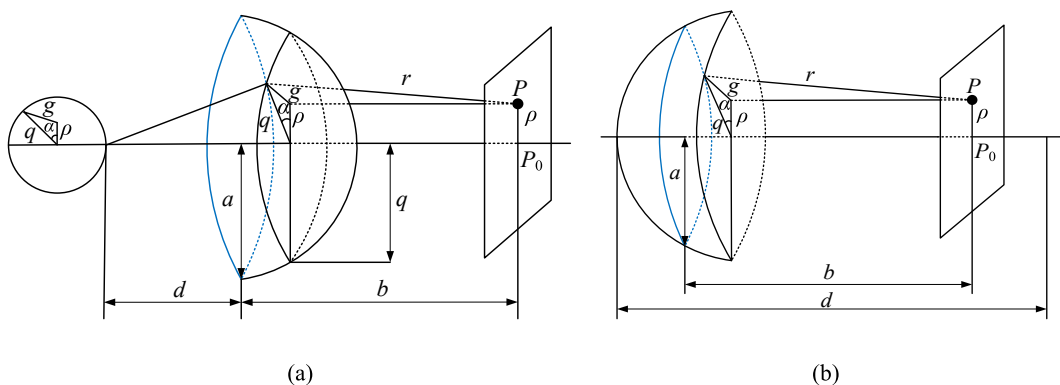
Fig. 1. Schematic diagram of the propagation process of divergent and convergent spherical waves. (a) is the propaganda process of divergent spherical wave, (b) is the propaganda process of convergent spherical wave.

This study proposes an improved intensity distribution calculation method for conventional optical microscopes. Our current approach is novel in several ways and provides an improved intensity transmission and distribution calculation method for the conventional optical microscopes and a mathematical relationship between the blur degree and camera parameters. First, the model of incident light intensity distribution and propagation in a complex microscopic optical system is established considering several actual optical system parameters based on the fluctuation equations in free space and the property description of Fresnel circular aperture diffraction in physical optics. Second, a simplified mathematical relationship between the blur kernel and camera parameters is quantitatively developed by analyzing the property of intensity distribution and blurring imaging, and the three-dimensional (3D) blurring properties in the optical imaging process is analyzed by comparing the variation law of the blurring property with respect to different wavelengths. Third, a connection between the diffractive optics and geometric optics is constructed by summarizing and generalizing the 3D blurring property curve of each monochromatic light source. Finally, a series of simulations and experiments are conducted to verify the proposed method.

2. Intensity distribution based on Fresnel diffraction

The divergent- and convergent wave models in Fresnel diffraction established based on the Fresnel Kirchhoff diffraction formula in the study in Ref. [25] are shown in Fig. 1 (a) and (b) respectively, where d is the distance from the light source to the circular hole; b is the distance from the circular hole to the receiving plane; a is the radius of the circular hole, ρ is the distance from P to P_0 on the optical axis, q is the distance from any point on the wave front to the center of the wave front, and α is the angle between q and ρ.(a) (b)

Then, r can be approximated as,

$$r \approx b + \frac{M}{2b}q^2 + \frac{\rho^2}{2b} - \frac{q\rho}{b}\cos\alpha \ , \ M = \frac{d \pm b}{d} \tag{1}$$

where $\cos\alpha$ can be expressed as,

$$\cos\alpha = \frac{q^2 + \rho^2 - g^2}{2q\rho} \tag{2}$$

With Eqs. (1) and (2), E_P is calculated by,

$$E_P = E_0 \exp\left[\frac{ik}{2b}\left(\rho^2 + Ma^2\right)\right] \times \sum_{n=1}^{\infty}\left(-i\frac{Ma}{\rho}\right)^n J_n\left(\frac{kqa}{b}\right) \tag{3}$$

$$E_0 = \frac{\exp(ik(d \pm b))}{d \pm b} \tag{4}$$

where "+" corresponds to the divergent wave in Fig. 1(a); "-" corresponds to the convergent wave in Fig. 1(b).

From Eq. (3) it can be found that the amplitude of a convergent wave travelling in an open optical diffraction system can be calculated, and when $d = b$, the wave emitted from a light source is converged into a point on the receiving plane, which is similar to the imaging process in a closed optical imaging system. Therefore, in the following section, we will analyze the convergent characteristics of the light source in the imaging process based on Eq. (3), model the intensity distribution in an optical imaging system and measure the PSFs when different practical camera parameters are considered.
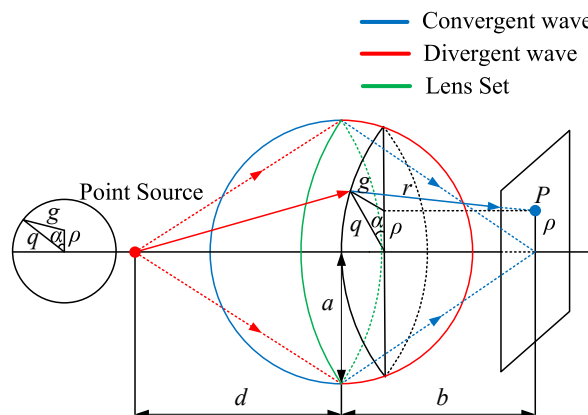
Fig. 2. Schematic diagram of the transformation process of spherical waves in an optical system.

3. Modelling the intensity distribution and 3D blur property

3.1. Intensity distribution model during imaging

To analyze the wave propagation process of a light source in an optical system, the divergent- and convergent spherical waves in Fig. 1 (a) and (b) are combined. The result is shown in Fig. 2, where the propagation process from the light source to the lens complies with the properties of divergent waves, and the propagation process from the lens to the imaging plane complies with the properties of convergent waves.

For an optical imaging system, the ideal object distance d_0 and the ideal image distance b_0 are easily to be known. When the image plane moves Δb along the optical axis, $\Delta b = b - b_0$. E_P is easily calculated with Eq. (3), where M and E_0 in Eq. (4) can be transformed as Eq. (5),

$$M = \frac{\Delta b}{b_0} \ , \ E_0 = \frac{\exp(ik\Delta b)}{\Delta b} \tag{5}$$

However, for a practical optical microscope with a high magnification factor, the image distance is usually fixed, while the object distance is a very flexible parameter. Therefore, to convert Δb in Eq. (3) into Δd ($\Delta d = d - d_0$), referred to as the distance variation relative to the ideal object distance, the imaging process in the geometry optics is used, as shown in Fig. 3.

First, when the object distance is fixed to d_0 and the variation of the image distance is Δb, the source point image on the image plane is a circular spot χ_1 with a diameter of p_1. From the geometric relations in Fig. 4, we can obtain Eq. (6),

$$\frac{p_1}{D} = \frac{\Delta b}{b_0} \tag{6}$$

where D is the height of the observed object.

Then, we fix the image distance to b_0 and move the observed object Δd along the optical axis, as a result, another circular spot χ_2 with a diameter of p_2 appears on the image plane, which can be calculated it by,

$$\frac{p_2}{h} = \frac{b_0}{d_0} \tag{7}$$

where h is the radial change of the optical path after depth changing, and it can be denoted as,

$$\frac{h}{D} = \frac{\Delta d}{d_0 + \Delta d} \tag{8}$$

Introduce Eq. (8) into Eq. (7), we can obtain Eq. (9),

$$p_2 = \frac{\Delta d b_0 D}{d_0 (d_0 + \Delta d)} \tag{9}$$

Let $p_1 = p_2$, we can obtain the relationship between Δb and Δd as Eq. (10),

$$\frac{\Delta b}{b_0} = \frac{\Delta d b_0}{d_0 (d_0 + \Delta d)} \tag{10}$$

Therefore,

$$\Delta b = \frac{\Delta d b_0^2}{d_0 (d_0 + \Delta d)} \tag{11}$$
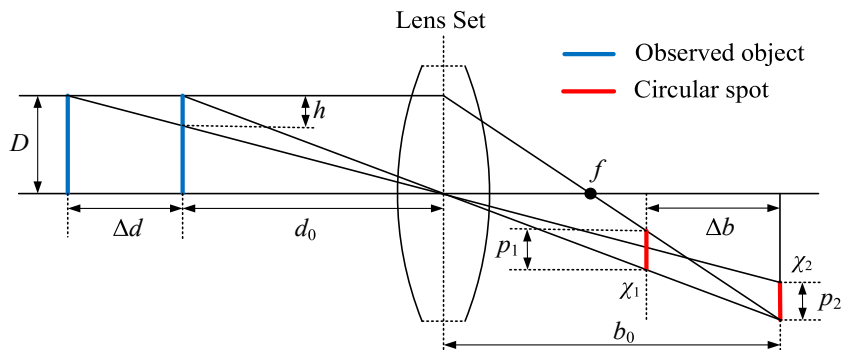
Fig. 3. Schematic diagram of microscope imaging in geometry optics.
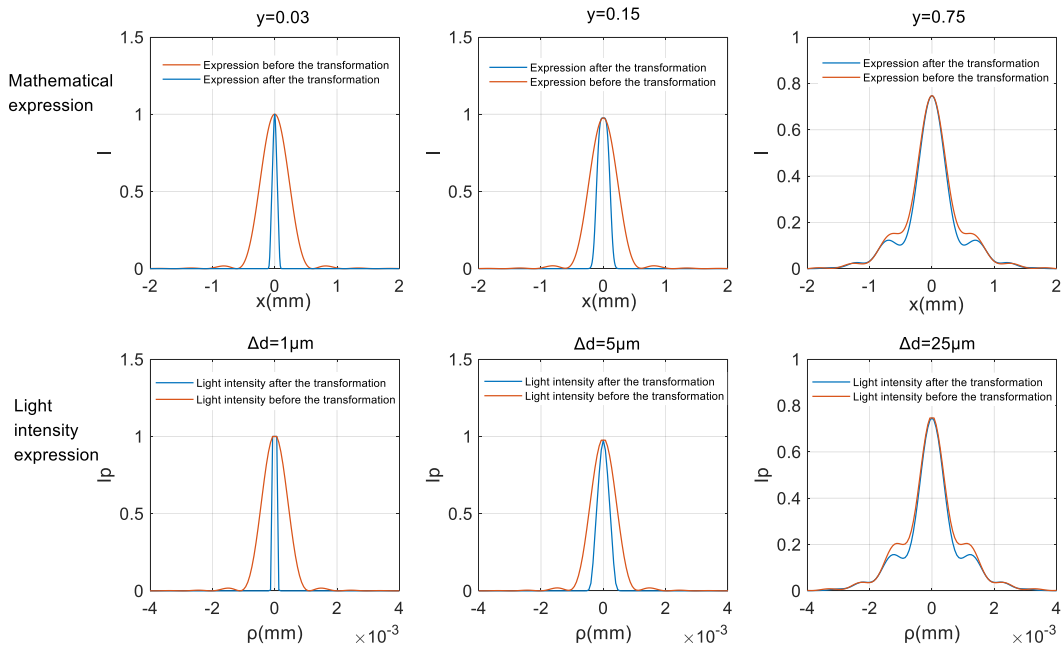
Fig. 4. Comparison of light intensity distributions before and after transformation.

According to the Gaussian imaging formula in the geometry optics, d_0 is equal to,

$$d_0 = \frac{b_0 f}{b_0 - f} \tag{12}$$

where f denotes the focal length of the imaging system.

Bring Eq. (12) into Eq. (11), Δb can be denoted as Eq. (13),

$$\Delta b = \frac{\Delta d \xi^2 b_0}{b_0 f^2 + \xi f \Delta d} \tag{13}$$

where $\xi = b_0 - f$.

Therefore, r in Eq. (1) can be transformed into Eq. (14),

$$r = \delta + \frac{\Delta d \xi^2}{2 b_0 \delta f (f + \delta \Delta d)} q^2 + \frac{\rho^2}{2\delta} - \frac{q\rho \cos \alpha}{\delta} \tag{14}$$

where the expression of δ is Eq. (15),

$$\delta = b_0 - \Delta b = b_0 \left(1 - \frac{\Delta d \xi^2}{f(b_0 f + \xi \Delta d)} \right) \tag{15}$$

Finally, E_P can be denoted as Eq. (16),

$$E_P = E_0 \exp\left[iCN\pi \left(1 + \frac{\rho^2}{Ca^2} \right) \right] \times \sum_{n=1}^{\infty} \left(-\frac{iCa}{\rho} \right)^n J_n\left(\frac{k\rho a}{\delta} \right) \tag{16}$$

where $N = a^2 / \lambda \delta$; $C = \xi^2 \Delta d / (b_0 f^2 + \xi f \Delta d)$, and E_0 is denoted as Eq. (17),

$$E_0 = \frac{\exp(ikCb_0)}{Cb_0} \tag{17}$$

Then, light intensity I at point P can be calculated by,

$$I = E_P \cdot E_P{}^* \tag{18}$$

Combined with Eq. (16), Eq. (18) is expressed as Eq. (19),

$$I = I_0 \cdot \sum_{n=1}^{\infty} \left(-i\frac{Ca}{\rho}\right)^n J_n\left(2N\pi\frac{\rho}{a}\right) \cdot \sum_{n=1}^{\infty} \left(i\frac{Ca}{\rho}\right)^n J_n\left(2N\pi\frac{\rho}{a}\right) \tag{19}$$

where $I_0 = E_0 \cdot E_0^*$.

The normalized I is equal to,

$$I_P = \sum_{n=1}^{\infty} \left(-i\frac{Ca}{\rho}\right)^n J_n\left(2N\pi\frac{\rho}{a}\right) \cdot \sum_{n=1}^{\infty} \left(i\frac{Ca}{\rho}\right)^n J_n\left(2N\pi\frac{\rho}{a}\right) \tag{20}$$

Due to the property of the Bessel function, as n rises, the amplitude of the function gradually decreases. In this study, n is set to 100.

Therefore, if the camera parameters of the imaging system are all known, including f, a, λ, b_0 and d_0, the intensity at P is a function of Δd because both C and N are related with Δd. In other words, Eq. (20) can be used to study the intensity distribution of a source point when its depth is changing. However, the relationship between the distribution property and the depth variation is still difficult to be analyzed because it is still a complicated infinite summation function of the Bessel functions. Therefore, it is necessary to simplify it to be an analyzable equation.

3.2. Improvement on the intensity distribution model

First, according to the property of the Bessel function, the following equations Eq. (21) and Eq. (22) are satisfied [42],

$$J_{-n}(x) = (-1)^n J_n(x) \tag{21}$$

$$\sum_{n=-\infty}^{\infty} J_n(x)y^n = J_0(x) + \sum_{n=1}^{\infty} (-y)^n J_n(x) + \sum_{n=1}^{\infty} y^n J_n(x) \tag{22}$$

The summation of the n-th Bessel functions can be transformed into Eq. (23),

$$\sum_{n=-\infty}^{\infty} y^n J_n(x) = \exp\left[\frac{x}{2}\left(y - \frac{1}{y}\right)\right] \tag{23}$$

With the property of orthogonal polynomial [42], we obtain,

$$\frac{\sum_{n=1}^{\infty} \left(-\frac{1}{y}\right)^n J_n(x)}{\sum_{n=1}^{\infty} (y)^n J_n(x)} = \frac{\exp\left(-\frac{1}{y^2}\right) - 1}{e - 1} \tag{24}$$

where e is the natural constant.

Therefore, Eq. (22) can be transformed into,

$$\sum_{n=-\infty}^{\infty} y^n J_n(x) = J_0(x) + \left(1 + \frac{\exp\left(-\frac{1}{y^2}\right) - 1}{e - 1}\right) \sum_{n=1}^{\infty} y^n J_n(x) \tag{25}$$

Finally, Eq. (25) can be simplified into a mathematical function without infinite summation,

$$I_P = (e - 1)^2 \frac{1 - J_0(x)\exp\left[\frac{x}{2}\left(y - \frac{1}{y}\right)\right] - J_0(x)\exp\left[-\frac{x}{2}\left(y - \frac{1}{y}\right)\right] + J_0^2(x)}{\left(\exp\left(-\frac{1}{y^2}\right) + e - 2\right)^2} \tag{26}$$

Replace x and y in Eq. (26) with the parameters as follows,

$$x = 2N\pi\frac{\rho}{a}, y = \frac{Ca}{\rho}, C = \frac{\xi^2\Delta d}{b_0 f^2 + \xi f\Delta d} \tag{27}$$

Then, I_P can be denoted as,

$$I_P = (e - 1)^2 \cdot \left(\frac{1 - J_0\left(2N\pi\frac{\rho}{a}\right)e^- - J_0\left(2N\pi\frac{\rho}{a}\right)e^+ + J_0^2\left(2N\pi\frac{\rho}{a}\right)}{\left(\exp\left(\frac{\rho^2}{C^2 a^2}\right) + e - 2\right)^2}\right) \tag{28}$$

$$e^- = \exp\left[-iCN\pi\left(1 + \frac{\rho^2}{C^2 a^2}\right)\right], e^+ = \exp\left[iCN\pi\left(1 + \frac{\rho^2}{C^2 a^2}\right)\right]$$

From Eq. (28), we can find that the intensity at P be calculated using a simpler function. However, the transformation in Eq. (24) bases on the assumption that the value of variable y is not much smaller than 1. To analyze the error of this assumption, we calculated I_P with Eqs. (20) and (26) when y was smaller than 1. For comparison, the intensity with different Δd values corresponding to y was also calculated with Eqs. 27 and 28 and our known camera parameters. The results are shown in Fig. 4, where the light intensity distribution before and after transformation was far from each other when y or Δd were very small, while with the increasing of Δd or y, the difference between them decreased. Because the intensity distribution with respect to small depth variation is very important for measurement of the blur property resulted from optical diffraction, it is necessary to improve this transformation and reduce the difference between Eq. (20) and Eq. (28) by introducing a complement factor.

To solve this problem, the distributions after transformation based on Eq. (24) can be amplified laterally here, where the parameter K is the lateral magnification with a guaranteed minimal root mean square error (RMSE) between the curves before and after amplification. Therefore, K related to y is introduced to adjust the changing speed of x, that is, x in Eq. (27) is replaced by x/K. Therefore, the light intensity distribution is calculated as,

$$
I_P = (e-1)^2 \cdot \frac{1 - J_0\left(2N\pi \frac{\rho}{Ka}\right)e_k^- - J_0\left(2N\pi \frac{\rho}{Ka}\right)e_k^+ + J_0^2\left(2N\pi \frac{\rho}{Ka}\right)}{\left(\exp\left(\frac{\rho^2}{C^2 K^2 a^2}\right) + e - 2\right)^2}
$$

$$
e_k^- = \exp\left[-iCN\pi\left(1 + \frac{\rho^2}{K^2 C^2 a^2}\right)\right], e_k^+ = \exp\left[iCN\pi\left(1 + \frac{\rho^2}{K^2 C^2 a^2}\right)\right]
$$

(29)

The relationship between K and y is showed in Fig. 5 (a) where we can find that when y is between -0.5 and 0.5, K greatly increases, while when y is more than 1, K is close to 1. Because Eqs. (26) and (28) have the same trend and lateral magnification before and after the transformation based on Eq. (24), K is independent on the camera parameters, and we can take it as an experienced parameter used in the intensity analysis of different optical microscopes. The specific values can be obtained from Table 1. Furthermore, the K values with respect to different Δd can be calculated with Eq. (27) using the data in Table 1 and the parameters of a practical system. The improvement result of Fig. 5 is shown as Fig. 5 (b), where we can find that when Δd was less than 0.001 mm, K was greatly increased, while when Δd was more than 0.001 mm, K was close to 1. It implies that K is effectively to compensate the gap before and after transformation in Eq. (24) when the depth variation is small. The intensity distribution with K is shown in Fig. 6, where we can observe that the curves before and after transformation were close to each other.

3.3. Three-dimensional blur property in a microscope

To further study the mathematical relationship between the blur property and depth variation in an optical microscope, it is necessary to further simplify Eq. (29).

First, due to the fact that the translation of a function does not change its properties, $(\exp((\rho^2/K^2 C^2 a^2)+e\text{-}2))^{-2}$ in Eq. (29) has the same mathematical property to that of the function $(\exp(\rho^2/K^2 C^2 a^2))^{-2}$ which equals to a product of two Gaussian functions $\exp(-\rho^2/K^2 C^2 a^2)$. Furthermore, because the variation range of CK is mostly in the micrometer scale when the optical diffraction is researched, while the variation range of ρ is in the millimeter scale; therefore, in the variable $X = \rho/CKa$, the variation of CK caused by depth changing can be ignored and X is reasonably regarded as a variable of ρ. Then, according to the properties of Gaussian functions, $\exp((\rho^2/K^2 C^2 a^2)+e\text{-}2)^{-2}$ can be replaced with a Gaussian function, shown as,

(a)

(b)
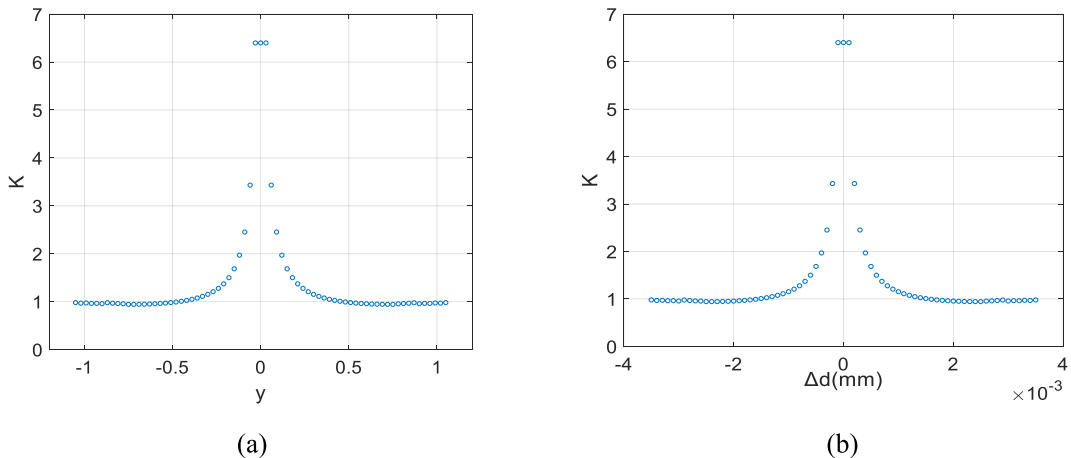
Fig. 5. The distribution of the parameter K. (a) shows the values of K that complements the deviation calculated in Eq. (26), (b) shows the values of K that complements the deviation calculated in Eq. (28).

Table 1
The corresponding relationship between y and K.

y	−0.45	−0.39	−0.33	−0.27	−0.21	−0.15	−0.09	−0.03	0
K	1.01	1.02	1.11	1.21	1.37	1.69	2.45	6.39	6.40
y	**0.03**	**0.09**	**0.15**	**0.21**	**0.27**	**0.33**	**0.39**	**0.45**	
K	6.39	2.45	1.69	1.37	1.21	1.11	1.05	1.01	
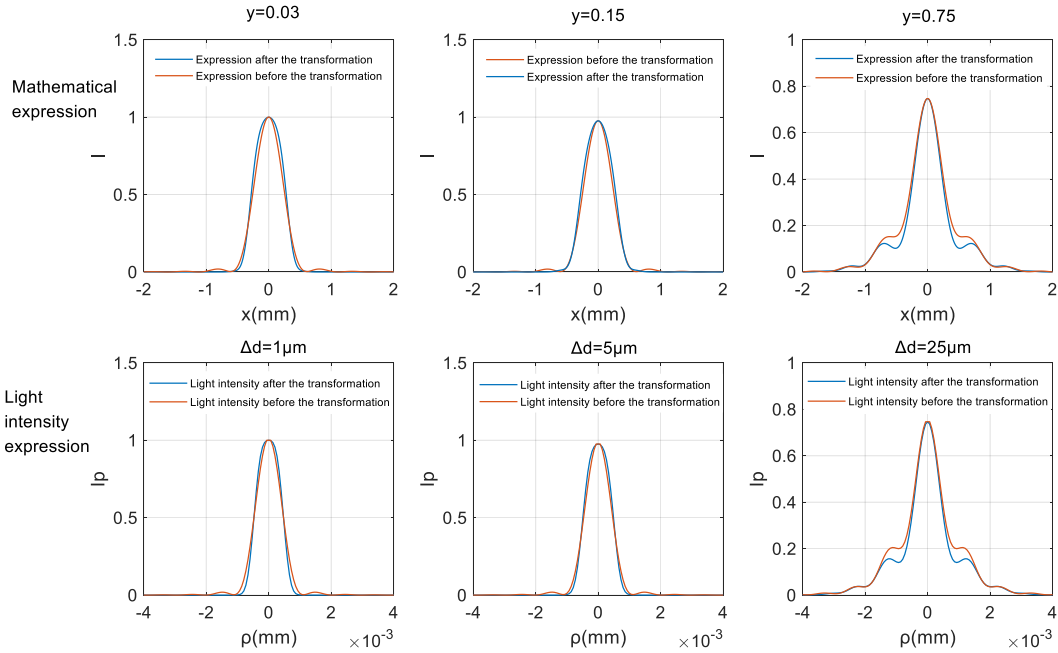
Fig. 6. Comparison of light intensity distribution with K before and after transformation.

$$\left(\exp\left(\frac{\rho^2}{C^2 K^2 a^2} \right) + e - 2 \right)^{-2} \approx A_1 \exp\left(-\frac{X^2}{2\varepsilon_1^2} \right) = A_1 \exp\left(-\frac{\rho^2}{2\varepsilon_1^2 C^2 K^2 a^2} \right) \tag{30}$$

As discussed previously, compared to ρ, the variation of Δd does not greatly influence the variance ε_1 and A_1 in Eq. (30). In other words, when the object distance changes in a small range, the variation of ε_1 and A_1 can be ignored. Therefore, ε_1 and A_1 can be taken as two constants. In practice, it is easy to obtain them with the camera parameters of a microscope because when we randomly choose a very small Δd, C and K in Eq. (30) are both known.

And Eq. (29) is transformed into,

$$I_P = A_1 (e-1)^2 \exp\left(-\frac{\rho^2}{2\varepsilon_1^2 C^2 K^2 a^2} \right)$$
$$+ A_1 (e-1)^2 J_0^2\left(2N\pi \frac{\rho}{Ka} \right) \exp\left(-\frac{\rho^2}{2\varepsilon_1^2 C^2 K^2 a^2} \right) \tag{31}$$
$$- 2A_1 (e-1)^2 J_0\left(2N\pi \frac{\rho}{Ka} \right) \exp\left(-\frac{\rho^2}{2\varepsilon_1^2 C^2 K^2 a^2} \right) \cos\left[CN\pi \left(1 + \frac{\rho^2}{K^2 C^2 a^2} \right) \right]$$

Since $\rho \ll a$, $\cos[CN\pi(1 + \rho^2/(K^2 C^2 a^2))] \approx 1$. Therefore, Eq. (31) can be expressed as,

$$I_P = A_1 (e-1)^2 \left(J_0\left(2N\pi \frac{\rho}{Ka} \right) - 1 \right)^2 \exp\left(-\frac{\rho^2}{2\varepsilon_1^2 C^2 K^2 a^2} \right) \tag{32}$$

To reduce the influence of the zero-order Bessel function in Eq. (32), its relationship with the Schläfli integral [37] is considered,

$$J_0(Z) = \frac{1}{2\pi i} \int_{-\infty}^{0+} \frac{\exp(t)}{t} \exp\left(-\frac{Z^2}{4t} \right) dt \tag{33}$$

Due to the existence of the limit of $\exp(t)/t$ in Eq. (33), the zero-order Bessel function can be regarded as a superposition of Gaussian functions with different standard deviations and different amplitudes. Therefore, the square of the zero-order Bessel function in Eq.

(32) can be replaced with a Gaussian function. Besides, the variation range of λK is much smaller than that of ρ in $Y = a\rho/\lambda K\delta$, and Y is then reasonably regarded as a variable of ρ. Because Δd is very small in a microscope, the value of δ is close to b_0. Therefore, $(J_0(2N\pi\rho/Ka) -1)^2$ can be replaced with $A_2\exp(-Y^2/2\varepsilon_2^2)$, that is,

$$\left(J_0\left(2N\pi\frac{\rho}{Ka}\right) - 1\right)^2 \approx A_2 \exp\left(-\frac{Y^2}{2\varepsilon_2^2}\right) = A_2 \exp\left(-\frac{a^2\rho^2}{2\varepsilon_2^2 K^2\lambda^2\delta^2}\right) \tag{34}$$

In Eq. (34), the change of $\lambda\delta$ in parameter N is small compared to the change of ρ and can be neglected, so the form of the zero-order Bessel function in Eq. (34) can be transformed into the form of an exponential function. Therefore, similar to Eq. (30), ε_2 and A_2 can also be taken as constants, which can be obtained if the practical camera parameters are known.

Therefore, Eq. (32) can be transformed into Eq. (35),

$$I_P = A_1 A_2 (e-1)^2 \exp\left(-\frac{a^2\rho^2}{2\varepsilon_2^2 K^2\lambda^2\delta^2}\right)\exp\left(-\frac{\rho^2}{2\varepsilon_1^2 C^2 K^2 a^2}\right) \tag{35}$$

Merge two Gaussian functions in Eq. Eqn 35, we get,

$$\begin{aligned} I_P &= A_1 A_2 (e-1)^2 \exp\left(-\frac{\rho^2\left(\varepsilon_1^2 C^2 a^4 + \varepsilon_2^2\lambda^2\delta^2\right)}{2\varepsilon_1^2\varepsilon_2^2\lambda^2 C^2 K^2 a^2\delta^2}\right) \\ &= A_1 A_2 (e-1)^2 \exp\left(-\frac{\rho^2}{2\sigma^2}\right) \end{aligned} \tag{36}$$

From Eq. (36), we can find that the light intensity at random point P can be calculated with a simple Gaussian function related to depth variation. The conclusion is consistent with the convention that the Gaussian function is usually used as the PSF in the macro scale imaging [43]. Moreover, because the blur degree can be evaluated by the variance of the PSF, the relationship between the blur kernel and depth variation can be mathematically calculated by,

$$\sigma = \frac{\varepsilon_1\varepsilon_2\lambda CKa\delta}{\sqrt{\varepsilon_1^2 C^2 a^4 + \varepsilon_2^2\lambda^2\delta^2}} \tag{37}$$

where ε_1 and ε_2 are known with the practical camera parameters, such as λ, a, f, b_0, d_0; and C, K, δ are all the parameters related with Δd.

Therefore, if we know the camera parameters of a practical microscope, it is easy to calculate its blur kernel when depth varies with Eq. (37). It implies that its 3D blur property is achieved through our relationship between the blur kernel and depth variation.

4. Simulation

In this section, a series of simulations were conducted to validate the light-intensity distribution model and the relationship between the blur kernel and depth variation proposed in this study. The following parameters were considered in the optical microscope system in our simulation: the ideal object distance: 34 mm; the ideal image distance: 48.57 mm; the focal length: 20 mm; the numerical aperture: 0.28; the system imaging resolution: 1 μm.
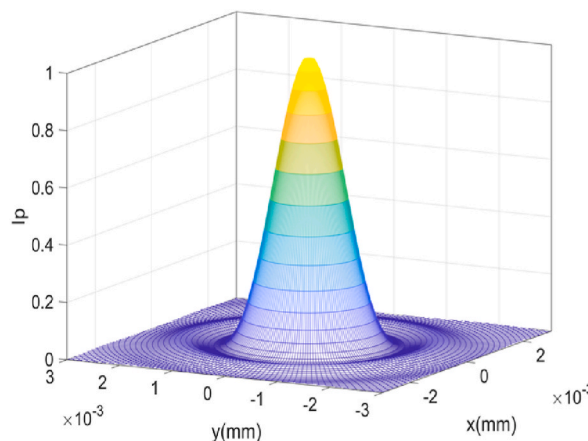
Fig. 7. Light intensity distribution on the imaging surface.

4.1. Simulation on intensity distribution of a source point

First, the light intensity distribution on the imaging surface was calculated with Eq. (29) when the point source was located at the ideal object distance. The results are shown in Fig. 7, where the x- and y axes represent the coordinates of the image plane. It can be observed that the intensity distributed unevenly in the central region of the Airy spot due to optical diffraction, and there were a series of rings with small intensity peaks around the main intensity peak. The intensity in each ring gradually decreased with an increasing in the distance between the rings to the center. This is qualitatively consistent with the energy distribution properties of optical diffraction in the physical optics.

To quantitatively verify the light intensity model proposed in this study, the Rayleigh criterion was introduced to calculate the theoretical imaging resolution, which was compared with the actual system resolution. First, according to the definition of the Rayleigh criterion, when the overlapping position intensity of the light intensity curves of two adjacent light sources accounts for 73.5% of the peak intensity of a single curve, the distance between their centers is the minimum resolution. In this study, the light intensity distribution curves at the ideal object distance position were calculated using Eq. (29). The light intensity distributions are shown in Fig. 8. The results in Fig. 8 show that, when the Rayleigh criterion was met, the distance between the two centers was 1100 nm, which was close to the practical system imaging resolution of 1 μm.

To further validate the intensity distribution model, a simplified formula to estimate the minimum resolution of a practical optical system is used,

$$\psi_{\min} = \frac{0.61\lambda}{NA} \tag{38}$$

where $\psi_{\min}$ is the resolution; NA is the numerical aperture of the objective lens.

The calculated resolution using Eq. (38) was 1159 nm, which was 59 nm different from the resolution calculated by our model. Therefore, the intensity distribution modelling method proposed in this study can be used to calculate the light intensity distribution in an optical imaging system.

4.2. Simulation on relationship between blur kernel and depth-variation

First, the light intensity distribution curves of the point sources with different depth variations were calculated in our simulation. The result is shown in Fig. 9 where Fig. 9 (a) is the 3D intensity distribution image and Fig. 9 (b) is the intercepted two-dimensional profile through the centers of these curves. From Fig. 10, we can observe that the peak of the light intensity curve without depth variation was the highest. As the depth variation increased, the peak light intensity gradually weakened, and the intensity of the sidelobes gradually increased. This is consistent with the law of energy conservation, that is, the energy of the central peak gradually decreases because it spreads to the secondary wave peaks. In fact, the energy dispersion from the main peak to the sidelobes is the essence of blurring imaging in an optical microscope, and the smaller the main peak energy, the more blurred the image. Therefore, it is reasonable to measure the energy variation pattern of the main peak to estimate the blur degree. Because the light intensity curves at different depths have a shape similar to that of a Gaussian function, whose standard variance is an effective factor to evaluate the energy distribution, we can fit these curves with Gaussian functions. The results are shown in Fig. 10, where we can see that the intensity curves with less depth variation were finely fitted; although the fitting error increased at the sidelobes with increasing of depth variation, the main peaks were still closely fitted.

After fitting, we chose the standard variance of each Gaussian function as the blur kernel of this depth position and then compared
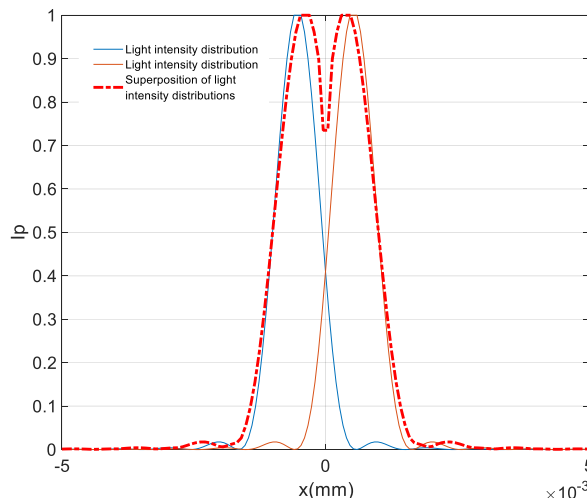
Fig. 8. Schematic diagram of Rayleigh criterion.
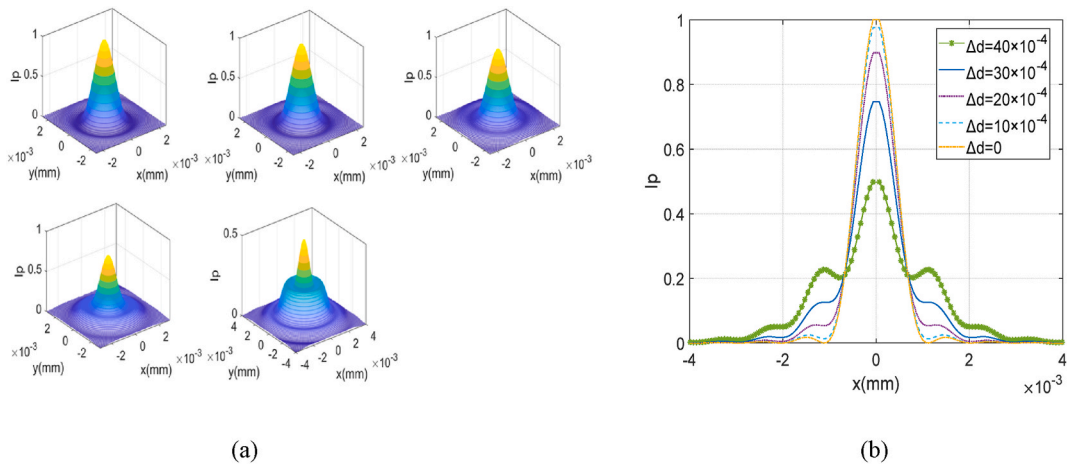
Fig. 9. 3D and 2D intensity distribution with different depth variations. (a) shows the 3D intensity distributions of light source when Δd takes different values, (b) shows the intercepted 2D profiles through the centers of the distributions in (a).
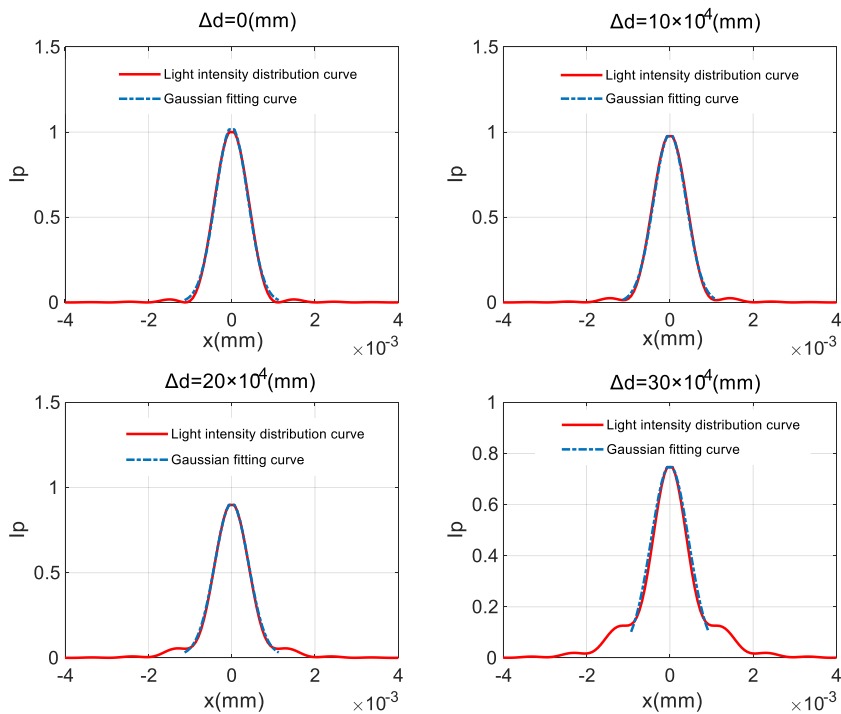
Fig. 10. Fitting the light intensity distribution curves with Gaussian functions.

with the relationship between the blur kernel and depth variation proposed in Eq. (37), where $\varepsilon_1 = 0.8490$ and $\varepsilon_2 = 0.2799$. The result is shown in Fig. 11, where Fig. 11 (a) shows the relationship curves between σ and Δd obtained by the curve fitting and our method, and Fig. 11 (b) is the distance between these two curves in Fig. 11 (a).

From Fig. 11, it can be observed that the shape of the Δd–σ curves was an inverted parabola with the symmetry axis representing the ideal object distance. The blur kernel values at the ideal object distance were the lowest, because the intensity was concentrated to the greatest extent at this position. When the depth variation was small, the blur kernel of these two methods increased smoothly; however, when the depth variation increased, the curve obtained by the Gaussian curve fitting was less smooth compared to that obtained by our method. This is because the ratio of the light intensity between the secondary and primary peaks increased with the increasing depth variation, resulting in a significant decrease in the precision of the curve fitting with a Gaussian function. In our method, the curve was calculated by a mathematical function, which was more robust. The distance between the fitted Δd–σ curve and the calculated Δd–σ curve did not vary significantly with depth variation, and the relative error to the Gaussian curve fitting was less
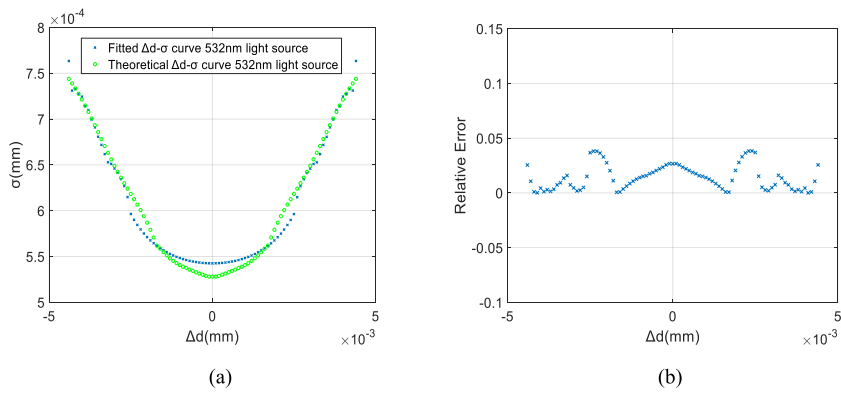
Fig. 11. The Δd–σ curves of the curve fitting and our method and their relative error. (a) shows the theoretical Δd–σ curve and Gaussian fitting Δd–σ curve of 532 nm light source, (b) shows the relative error between the theoretical Δd–σ curve and the Gaussian fitting Δd–σ curve.

than 0.05.

4.3. Simulation on 3D blur property under different conditions

● **Different wavelength**

To observe the difference between the Δd and -σ curves corresponding to different wavelengths, we fixed the other camera parameters and calculated the theoretical Δd–σ curves with Eq. (37) when the purple, green, and red lasers with a wavelength of 405 nm, 532 nm, and 635 nm, respectively, are selected. To compare the precision of these curves, we also calculated the intensity distribution at different depths with Eq. (29) and obtained the Δd–σ curves corresponding to different wavelengths using Gaussian curve fitting. The results are shown in Fig. 12 (a). To clearly observe the bending degree of each curve, the Δd–σ curves in Fig. 12 (a) were moved to the same coordinate origin, as shown in Fig. 12 (b).

From Fig. 12, the following conclusions can be drawn,

(1) For the Δd–σ curves with the same wavelength, the results of our theoretical 3D blur property calculation method in Eq. (37) and the intensity model in Eq. (29) combined with the Gaussian fitting were close to each other, proving that our mathematical relationship between the blur kernel and depth variation was accurate. Therefore, it is reasonable to use a Gaussian function to fit the PSFs when the depth variation is not large.
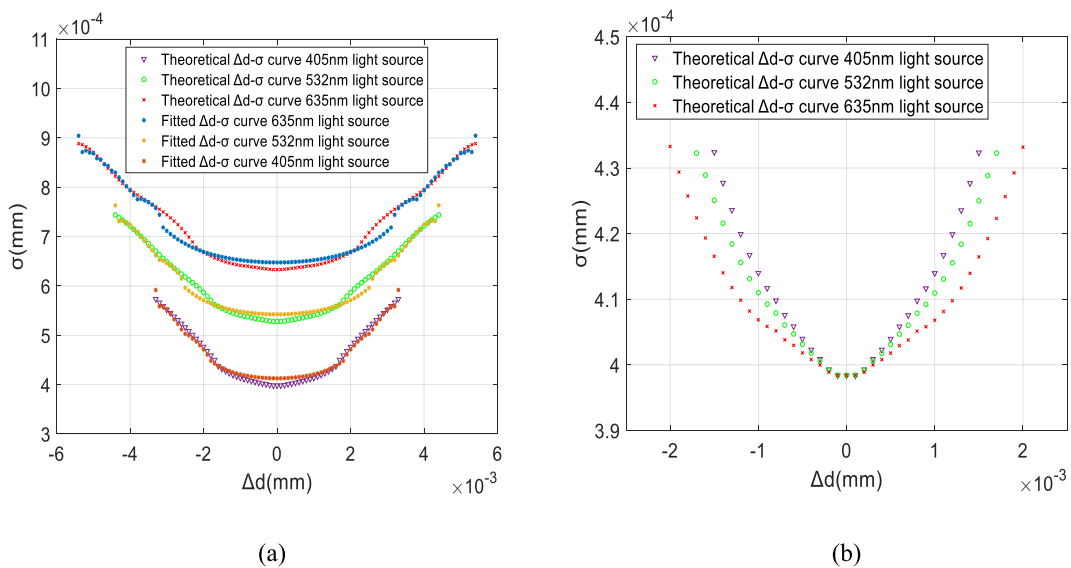
Fig. 12. Δd–σ curves corresponding to different light sources. (a) shows the theoretical Δd–σ curves and Gaussian fitting Δd–σ curves of different wavelength light sources, (b) shows the theoretical Δd–σ curves of different wavelength light sources at a same coordinate origin.

(2) When the wavelength was varied, the curve of the purple laser had the smallest σ values compared to the other two curves. This implies that the energy distribution of the purple laser is more concentrated. This result satisfies the conclusion that purple light has the highest resolution.

(3) When Δd was the same, the curve corresponding to the purple light source varied the most dramatically, followed by the green and red sources. Therefore, the purple light source with the shortest wavelength was the most sensitive to depth variation.

● **The boundary between diffraction blurring and defocused blurring**

In the geometric optics, the radius of a defocused spot can be calculated by Eq. (39),

$$\varsigma = \frac{1}{2} a b_0 \left| \frac{1}{f} - \frac{1}{b_0} - \frac{1}{d} \right| \tag{39}$$

When the Gaussian function is used as the PSF, the blur kernel σ equals to Eqn 40,

$$\sigma^2 = \eta^2 (\varsigma)^2 \tag{40}$$

where η is a scaling factor between the spot diameter and the blur kernel. It can be obtained in the calibration process.

Then, the Δd–σ curves in the geometric optics with different η values were compared with the Δd–σ curves of our 3D blur property model corresponding to different wavelengths, and the results are shown in Fig. 13. It can be observed that, although the Δd–σ curves of different light sources had different curvature degrees, they gradually converged to the Δd–σ curves of the geometric optics as the increasing of Δd. This is because, when Δd is small, optical diffraction is the dominant factor influencing the imaging result of the optical system. However, when Δd is sufficiently large, defocus plays a major role in imaging, thus resulting in a change in the blur kernel that meets the convex lens imaging theory in the geometric optics. Therefore, our model establishes a connection between the diffractive and geometric optics by summarizing and generalizing the properties of the Δd–σ curves of each monochromatic light source.

5. Experiment

To verify our mathematical light-intensity distribution model and Δd–σ curves established in this study, a series of experiments were conducted using our self-made optical microscopic system. The objective lens was a compound achromatic apochromatic lens from Navitar. Its maximum magnification and working distance were 12 × and 34 mm, respectively. The numerical aperture was 0.28, the resolution was 1 μm, the DOF was 3.5 μm. The CCD was Canadian PointGrey 1394B. The three-dimensional nano-positioning piezoelectric ceramic platform NPBIO300 from NPOINT, USA, was used. The platform was a three-axis XYZ control with a closed-loop travel of 300 μm, and an open-loop travel of 360 μm, a positioning accuracy of 2 nm, a frequency of 200 Hz and a rectification time of 20 ms.

5.1. Comparison of light intensity distribution

In our experiment, a Gaussian light source with a wavelength of 532 nm was used as the observation object, and its energy distribution properties on the imaging plane was measured and analyzed. We captured a series of Gaussian beam images at different depths, shown as Fig. 14.

To analyze the intensity distribution property of the light source, Fig. 14 (a) was converted into a grayscale image and normalized to achieved its intensity image, as shown in Fig. 15 (a), where it can be observed that there were multiple diminishing intensity rings around the central intensity peak, which is consistent with the result in our simulation. To compare the intensity distribution property of the Gaussian source with the calculation result of our model, we intercepted a two-dimensional profile through the center of Fig. 15 (a). The result is shown in Fig. 15 (b). From the results, we can see that our calculated intensity distribution curve was close to the actual intensity distribution of the Gaussian beam, especially near the main peak. To quantitatively compare them, we calculated the mean relative error (MRE) of two intensity curves. The MRE value of the entire main peak was 0.037.

5.2. Relationship between the blur kernel and depth variation

To validate the relationship between the blur kernel and depth variation of practical light sources, we extracted the intensity curves through the centers of the captured Gaussian beam images. Then, the intensity curves at each depth were fitted with a Gaussian function, and the blur kernel of each depth was obtained after fitting through two methods: 1) Directly extract the standard variance value from the fitted Gaussian functions; 2) Evaluate the standard variance values based on the three-sigma rule on covering area of the fitted Gaussian functions. Therefore, we obtained two practical Δd–σ curves after curve fitting and compared them with our theoretical Δd–σ curves. In this study, to validate our intensity model and the Δd–σ relationship, we used two theoretical Δd–σ curves: 1) Calculate the intensity distribution curves with Eq. (29) and fit them with Gaussian functions to extract their corresponding standard variance values; 2) Calculate the standard variance values with the depth information using the Δd–σ relationship in Eq. (37). The comparison results are shown in Fig. 16, where Fig. 16 (a) shows the Δd–σ curves of these four methods, and Fig. 16 (b) shows the relative error values between the theoretical Δd–σ curve calculated by our method, the fitted theoretical Δd–σ curve, and two practical Δd–σ curves.

From Fig. 16 (a), we can observe that these practical and theoretical Δd–σ curves had very close shapes, and comparatively the blur
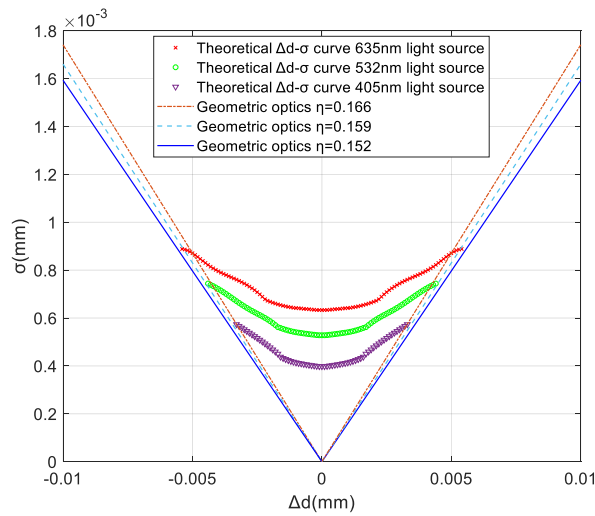
Fig. 13. Δd–σ curves in the diffractive and geometry optics.

(a)　　　　　　　　　　　(b)　　　　　　　　　　　(c)
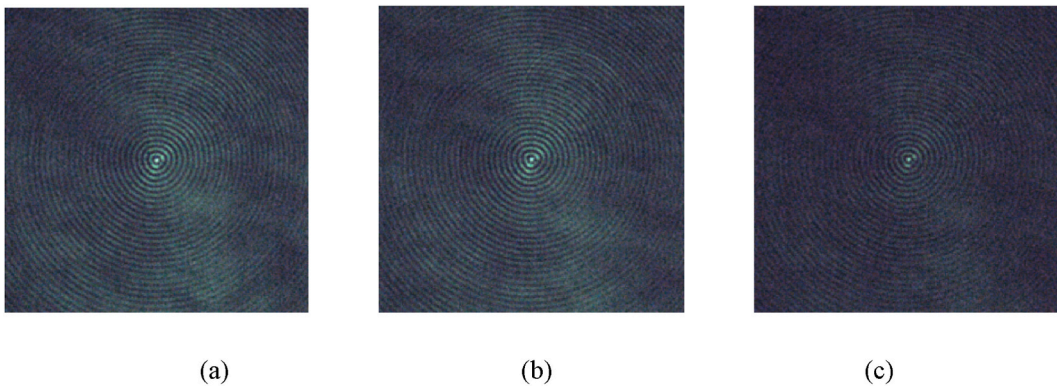
Fig. 14. A series of images of the green laser at different depths. (a) shows the diffraction image of 532 nm green laser source at $\Delta d = 0$ μm, (b) shows the diffraction image of 532 nm green laser source at $\Delta d = 2$ μm, (c) shows the diffraction image of 532 nm green laser source at $\Delta d = 4$ μm. (For interpretation of the references to colour in this figure legend, the reader is referred to the Web version of this article.)

(a)　　　　　　　　　　　(b)
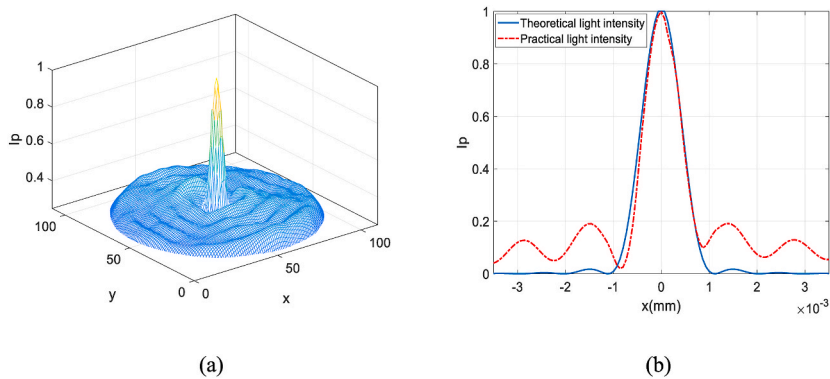
Fig. 15. Practical intensity distribution and its comparison with our theoretical distribution. (a) shows the 3D light intensity distribution of 532 nm green laser source at $\Delta d = 0$, (b) shows the comparison of intercepted 2D profile through the center of the distribution in (a) with the corresponding theoretical distribution. (For interpretation of the references to colour in this figure legend, the reader is referred to the Web version of this article.)
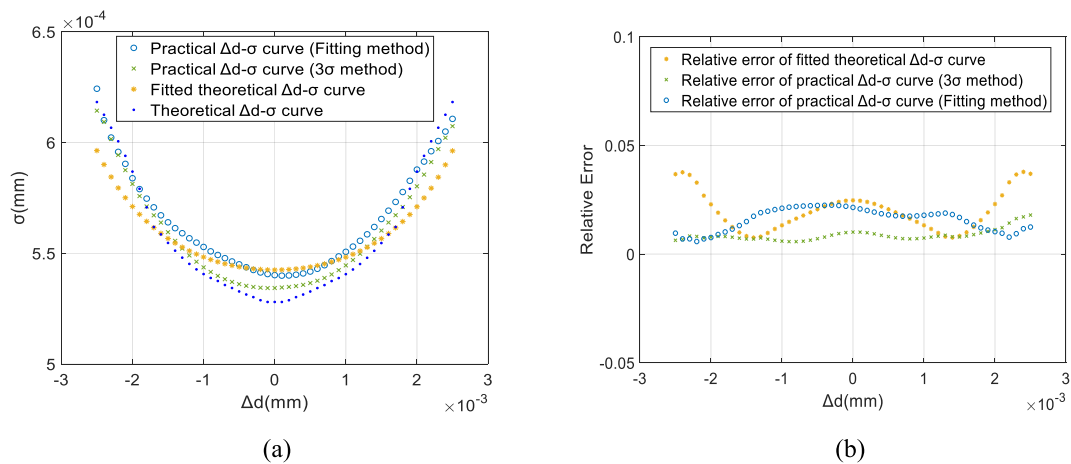
Fig. 16. Comparison of the practical and theoretical Δd–σ curves. (a) shows the comparison of the Δd–σ curves obtained by different four methods, (b) shows the relative error values between the theoretical Δd–σ curve calculated by our method, the fitted theoretical Δd–σ curve, and two practical Δd–σ curves.

kernels of the theoretical curve calculated with our method were the lowest, because there was no fitting noise or experimental noise in the calculation process. From Fig. 16 (b), it can be observed that the practical Δd–σ curve using the three-sigma method had the lowest relative error, because it was less sensitive to the small morphological changes in the intensity distribution curve; The MREs of the practical and theoretical Δd–σ curves using the Gaussian fitting were close to each other when the depth variation was small. When the depth variation was more than 0.002 mm, the MRE of the theoretical Δd–σ curve using the Gaussian fitting significantly increased. The MRE of the theoretical Δd–σ curve fitted with the Gaussian function, the practical Δd–σ curve measured using the three-sigma method and the practical Δd–σ curve fitted with the Gaussian function were 0.0198, 0.0087 and 0.0159, respectively. Therefore, our calculated Δd–σ curve was very close to the practical measured Δd–σ curve with the three-sigma method, which proves that the light intensity distribution model and the 3D blur property relationship proposed in this study are accurate and effective.

6. Conclusion

In this paper, a mathematical modelling method of light intensity distribution in an optical microscope considering optical diffraction and defocus was proposed. Furthermore, a 3D blur property calculation method with respect to depth variation was developed in an analytic mathematical form. First, an intensity distribution model containing the system parameters was established and simplified into an analytical expression based on Fresnel convergent spherical waves. Second, the 3D blur property between the blur kernel and camera parameters was mathematically developed according to the properties of the Bessel function and orthogonal polynomial. Third, the 3D blur property curves under different conditions were analyzed, and the connection between the diffraction optics and geometry optics was achieved through comparison with the Δd–σ curves in geometry optics. Finally, a series of simulations and experiments were conducted to verify the proposed methods.

Author contribution statement

All authors listed have significantly contributed to the development and the writing of this article. </p>

Data availability statement

Data will be made available on request.

Declaration of competing interest

The authors declare that they have no known competing financial interests or personal relationships that could have appeared to influence the work reported in this paper.

References

[1] J.W. Lichtman, J.A. Conchello, Fluorescence microscopy, Nat. Methods 2 (12) (2005) 910–920.

[2] H. Cheng, S. Tong, In vivo deep-brain imaging of microglia enabled by 3-photon fluorescence microscopy, Opt Lett. 45 (18) (2020) 5271–5274.

[3] M. Merlin, F. Andreas, Confocal fluorescence microscopy for geometry parameter measurements of submerged micro-structures, Opt Lett. 44 (5) (2019) 1237–1240.

[4] X. Yan, C. Liu, Single-defect phonons imaged by electron microscopy, Nature 589 (7840) (2021) 65–69.

[5] M. Herbig, P. Choi, D. Raabe, Combining structural and chemical information at the nanometer scale by correlative transmission electron microscopy and atom probe tomography, Ultramicroscopy 153 (2015) 32–39.

[6] Q. Zhou, X. Zhu, H.F. Li, Study on light intensity distribution of tapered-fiber in near-field scanning microscopy, Acta Physica Sinica -chinese edition 49 (2) (2000) 210–214.

[7] J. Moison, M.I. Abram, M. Bensoussan, Full mapping of optical noise in photonic devices: an evaluation by near-field scanning microscopy, Opt Express 16 (13) (2008) 9513–9518.

[8] K. Prusakov, B. Bagrov, Fluorescence imaging of cells using long range electromagnetic surface waves for excitation, Appl. Opt. 59 (16) (2020).

[9] X. Yi, P. So, Three-dimensional super-resolution high-throughput imaging by structured illumination STED microscopy, Opt Express 26 (16) (2018) 209–220.

[10] M. Born, P.C. Clemmow, D. Gabor, Principles of optics, Math. Gaz. 1 (370) (1999) 986–990.

[11] L. Chen, Z. Yang, L. Sun, Fast Autofocus of Microscopy Images Based on Depth-From-Defocus, IEEE/RSJ International Conference on Intelligent Robots & Systems IEEE, 2008.

[12] J.R. Alonso, A. Fernández, All-in-focus image reconstruction under severe defocus, Opt Lett. 40 (8) (2015) 1671–1681.

[13] S. Hell, W.S.J. Sahl, The 2015 super-resolution microscopy roadmap, J. Phys. D Appl. Phys. 48 (44) (2017) 443001.

[14] H. Fang, L. Qiu, Confocal light absorption and scattering spectroscopic microscopy monitors organelles in live cells with no exogenous labels, Proc. Natl. Acad. Sci. U.S.A. 104 (44) (2018) 17255–17260.

[15] M. Khorasaninejad, W.T. Chen, Metalenses at visible wavelengths: diffraction-limited focusing and subwavelength resolution imaging, Science 352 (6290) (2016) 1190–1194.

[16] B. Joseph Keller, Geometrical theory of diffraction, J. Opt. Soc. Am. 52 (2) (1962) 116–130.

[17] J. Durnin, J.H. Eberly, Diffraction-free beams, Phys. Rev. Lett. 58 (15) (1987) 1499–1501.

[18] J. Durnin, Exact solutions for nondiffracting beams. I. The scalar theory, J. Opt. Soc. Am. 4 (1987) 651–654.

[19] P. Sprangle, B. Hafizi, Comment on nondiffracting beams, Phys. Rev. Lett. 66 (6) (1991) 837, 837.

[20] S. Ruschin, Modified Bessel nondiffracting beams, J. Opt. Soci. Am. A 11 (12) (1994) 3224–3228.

[21] P.L. Overfelt, C.S. Kenney, Comparison of the propagation characteristics of Bessel, Bessel-Gauss, and Gaussian beams diffracted by a circular aperture, J. Opt. Soci. Am. A 8 (5) (1991) 732–745.

[22] H. Urey, Spot size, depth-of-focus, and diffraction ring intensity formulas for truncated Gaussian beams, Appl. Opt. 43 (3) (2004) 620–625.

[23] R. Suter, D. Hennessy, C. Xiao, Forward modeling method for microstructure reconstruction using x-ray diffraction microscopy: single-crystal verification, Rev. Sci. Instrum. 77 (12) (2006) 1363–1367.

[24] S. Larouche, D.R. Smith, Reconciliation of generalized refraction with diffraction theory, Opt Lett. 37 (12) (2012) 2391–2393.

[25] P. Wang, Y.G. Xu, W. Wang, Analytic expression for Fresnel diffraction, J. Opt. Soci. Am. Opt. Im. Sci. Vis. 15 (3) (1998) 684–688.

[26] B.H. McCormick, D.M. Mayerich, Three-dimensional imaging using knife-edge scanning microscopy, Microsc. Microanal. 10 (2) (2004) 1466–1467.

[27] J. Yang, Z. Zhang, Q. Cheng, Resolution enhancement in micro-XRF using image restoration techniques, J. Anal. At. Spectrom. 37 (4) (2022).

[28] S. Mehravar, B. Cromey, K. Kieu, Characterization of multiphoton microscopes by non-linear knife-edge technique, Appl. Opt. 59 (22) (2020).

[29] B. Bianco, A. Diaspro, Analysis of three-dimensional cell imaging obtained with optical microscopy techniques based on defocusing, Cell Biophys. 15 (3) (1989) 189–199.

[30] C. Sheppard, I.J. Cooper, Fresnel diffraction by a circular aperture with off-axis illumination and its use in deconvolution of microscope images, J. Opt. Soci. Am. A Opt. Im. Sci. Vision 21 (4) (2004) 540–545.

[31] D. Mas, J. Garcia, C. Ferreira, Fast algorithms for free-space diffraction patterns calculation, Opt Commun. 164 (4–6) (1999) 233–245.

[32] U. Agero, C.H. Monken, C. Ropert, Cell surface fluctuations studied with defocusing microscopy, Phys. Rev. E - Stat. Nonlinear Soft Matter Phys. 67 (5 Pt 1) (2003), 051904.

[33] D. Agard, Optical sectioning microscopy: cellular architecture in three dimensions, Annu. Rev. Biophys. Bioeng. 13 (1984) 191–219.

[34] J.W. Shaevitz, D.A. Fletcher, Enhanced three-dimensional deconvolution microscopy using a measured depth-varying point-spread function, J. Opt. Soc. Am. A Opt. Im. Sci. Vision 24 (9) (2007) 2622–2627.

[35] A.V. Diezmann, M.Y. Lee, M.D. Lew, Correcting field-dependent aberrations with nanoscale accuracy in three-dimensional single-molecule localization microscopy, Optica 2 (11) (2015) 985.

[36] J.L. Beverage, R.V. Shack, M.R. Descour, Measurement of the three-dimensional microscope point spread function using a Shack-Hartmann wavefront sensor, J. Microsc. 205 (Pt 1) (2010) 61–75.

[37] W.S. Lee, G. Lim, W.C. Kim, Investigation on improvement of lateral resolution of continuous wave STED microscopy by standing wave illumination, Opt Express 26 (8) (2018) 9901–9919.

[38] P. Sarder, A. Nehorai, Deconvolution methods for 3-d fluorescence microscopy images, IEEE Signal Process. Mag. 23 (3) (2006) 32–45.

[39] J. Kim, S. An, S. Ahn, B. Kim, Depth-variant deconvolution of 3d widefield fluorescence microscopy using the penalized maximum likelihood estimation method, Opt Express 21 (23) (2013), 27668.

[40] N. Patwary, C. Preza, Image restoration for three-dimensional fluorescence microscopy using an orthonormal basis for efficient representation of depth-variant point-spread functions, Biomed. Opt Express 6 (10) (2015) 3826–3841.

[41] C. Roider, R. Heintzmann, R. Piestun, A. Jesacher, Deconvolution approach for 3d scanning microscopy with helical phase engineering, Opt Express 24 (14) (2016) 15456–15467.

[42] J. Marmey, A. Lacroix, A Treatise on the Theory of Bessel Functions, Cambridge University Press, 1944, pp. 160–193.

[43] E. Maalouf, Contribution to Fluorescence Microscopy, 3D Thick Samples Deconvolution and Depth-Variant PSF, Mulhouse, 2010, pp. 26–30.